

Supporting Information

Developing Dynamic Ion Transport Channels in Polymer Solid Electrolytes for High-Performance Lithium Metal Batteries

Qiang Lv^a, Li-an Li^b, Xi Zhang^c, Runqi Wang^d, Ning Wen^d, Lijuan Xue^{e,f}, Haimei Wang^{a,d,}, Lei Shen^{g,j}, Dairong Chen^d, Francesco Ciucci^{h,i}, and John Wang^{a,j}.*

Dr. Q. Lv, Prof. J. Wang, Dr. H. M. Wang.

^a Department of Materials Science and Engineering, National University of Singapore, Singapore 117574, Republic of Singapore.

Email: whm312a@gmail.com (H.M. Wang)

L. A. Li

^b School of Ocean, Yantai University. Yantai, Shandong 264005, China.

Dr. X. Zhang

^c China University of Geosciences (Beijing), No. 29 Xueyuan Road, Haidian District, Beijing Municipality, P.R. China.

R. Q. Wang, Dr. N. Wen, Dr. H. M. Wang, Prof. D. R. Chen.

^d School of Chemistry and Chemical Engineering, Shandong University, Jinan, Shandong 250100, China.

Prof. L.J. Xue

^e School of Physics and Electrical Engineering, Linyi University, Linyi 276000, P. R. China;

^f Department of Physics, City University of Hong Kong, Hong Kong SAR, China.

Prof. L. Shen

^g Department of Mechanical Engineering, National University of Singapore, Singapore 117575, Republic of Singapore.

Prof. Francesco Ciucci

^h University of Bayreuth, Chair of Electrode Design for Electrochemical Energy Systems, Weiherstraße 26, 95448 Bayreuth, Germany.

ⁱ University of Bayreuth, Bavarian Center for Battery Technology (BayBatt), Universitätsstraße 30, 95447 Bayreuth, Germany.

Prof. L. Shen, Prof. J. Wang

^j National University of Singapore (Chongqing) Research Institute, Chongqing Liang Jiang New Area, Chongqing 401120, China.

2. Experimental Section

2.1 Materials

Hydroxyapatite (HAP, 99%, 10 nm) and PVDF-HFP (M=350000) were procured from Macklin. Sulfone (SL, >99.0%), 2,2'-Azobis(2-methylpropionitrile) (AIBN, 98%), 1-Methyl-2-pyrrolidinone (NMP, >99.5%) and Acetone (>99.5%), Bis(trifluoromethanesulfonyl)imide lithium salt (LiTFSI) were procured from Aladdin and stored in the glove box for later use. 2,2,2-Trifluoroethyl methacrylate (TFEMA) and 2,2,2-Trifluoroethyl Acrylate (TFEAA, stabilized with MEHQ, >98.0%), Polyethylene glycol (PEGDA, average Mn of 6000) were obtained from Aladdin and stored in refrigerator before use.

2.2 Preparation of PVDF-HFP/HAP nanofiber membranes

PVDF-HFP/HAP nanofiber membrane was fabricated by electrospinning technique. The electrospinning precursor solution was prepared by dissolving PVDF-HFP into the mixture of NMP and Acetone mixed solution. Then, 3 wt% HAP was added in the above mixed solution, and then ultrasonicated for 2 h and stirred at room temperature (RT) for 12 h. Subsequently, the uniform solution was then stored in a syringe with stainless-steel needle. The electrospinning process was carried out with a receive distance of 15 cm and the flowing speed of 10 $\mu\text{L min}^{-1}$ at the voltage of 15 kV. Finally, the as-prepared fiber membrane was further dried at 80 °C for 12 h to remove the residual solvent and cut into 16 mm diameter wafers for further utilization.

2.3 Fabrication of solid polymer electrolytes (SPEs)

Initially, 0.0045 mol LiTFSI with varying SL content (0, 0.0045, 0.009, 0.0135 mol) were respectively mixed to form different salt solutions. Then, a solution comprising 0.006 g AIBN, 0.09 g PEGDA, 1.5ml TFEMA, 1.5ml TFEAA and aforementioned salt solution were subjected to stirring at RT for 1 h, forming homogeneous solution, labeled as *in situ*-P, *in situ*-SL1, *in situ*-SL2, or *in situ*-SL3. Simultaneously, 80 μL precursor solution was dropped onto the PVDF-HFP/HAP fiber membranes supported by a glass plate. Then, the above fiber membranes containing the precursor solution was transferred to the heating chamber in the glove box and pre-heated at a constant temperature of 60 °C for 30 min to remove gas produced during the polymerization process and pre-cure the polymer monomer (which reduced the free monomers that may cause unwanted side reactions with Li,

while left the polymerization reaction unfinished), and then the fiber membranes were assembled into the coin cells. After this, the assembled cells were heated at a constant temperature of 60 °C for 5 h to gain the *in situ*-based SPEs. All the aforementioned procedures were conducted inside argon-filled glove box.

2.4 Material characterization

The morphology of prepared SPEs was characterized by Scanning electron microscopy (SEM, Merlin compact, Germany). Fourier transform infrared (FTIR, Nicolet is50, America) in an attenuated total reflection (ATR) mode were used to examine reaction mechanism. The dissociation of Li salt in synthesized SPEs was characterized by Raman spectroscopy (inVia-Reflex, Renishaw) and solid-state ^7Li nuclear magnetic resonance (NMR) spectra with a Bruker 600 MHz NMR spectrometer. X-ray diffraction (XRD, BRUKER) and differential scanning calorimetry (DSC, NETZSCH DSC 214) were utilized to study the phase structures of the prepared SPEs. The thermogravimetric (NETZSCH TG 209) analysis and burning tests were conducted to assess the thermal stability and fireproof properties of prepared SPEs. The tensile strength of synthesized SPEs was studied by universal mechanical testing machine (Zwick/Roell Z1.0) and the tensile strength was considered to be the stress value at the maximum of the curve. Additionally, X-ray photoelectron spectroscopy (XPS, ESCALAB 250Xi, America) were employed to identify the elemental species at the electrolyte/electrode interface after cycling of the Li anode and NCM cathode. Finally, the HRTEM images of the cycled NCM cathodes were characterized by HRTEM (FEITalos, F200X, America). Time-of-flight secondary ion mass spectrometry (TOF-SIMS, PHI Nano ToF2) was employed to study the surface composition of the Li anode. For depth profiling, a Bi^+ ion beam was used to analyze $200\ \mu\text{m} \times 200\ \mu\text{m} \times 100\ \mu\text{m}$ areas while a Cs^+ ion beam was used to sputter $400 \times 400\ \mu\text{m}^2$ areas centered around the analyzed areas.

PFG-NMR measurements were performed on a Bruker AVANCE NEO 500WB spectrometer equipped with a Diff50 probe (maximum gradient strength $1689\ \text{G cm}^{-1}$) at 25 °C. Samples were sealed under inert atmosphere in 5 mm quartz ampules. For ^7Li diffusion, we employed a stimulated-echo pulse sequence with two identical gradient pulses ($\delta = 1.0\ \text{ms}$) separated by $\Delta = 20\ \text{ms}$. For ^{19}F diffusion, the same sequence and gradient pulse duration ($\delta = 1.0\ \text{ms}$) were used, with a separation time

of $\Delta = 25$ ms. The PFG-NMR diffusion equation is based on the Stejskal-Tanner formula¹:

$$I(g) = I_0 \exp \left[-\gamma^2 g^2 \delta^2 \left(\Delta - \frac{\delta}{3} \right) \right] \quad (1)$$

where γ is the gyromagnetic ratio, g is the gradient amplitude, δ is the gradient pulse duration, and Δ is the diffusion time. By choosing δ and Δ appropriately for the ^7Li and ^{19}F signals, we obtained D_{Li^+} and D_{TFSI^-} (TFSI⁻ anion) directly.

2.5 Electrochemical measurement

Solid-state lithium metal batteries (SSLMBs) were assembled in the glove box using the CR2025 coin cells without additional liquid additives. The ionic conductivity at RT of the *in situ*-based SPEs was evaluated through electrochemical impedance spectroscopy (EIS) measurements by electrochemical workstation (CHI 660e, Shanghai CHI Inc, China) in stainless steel SS||SPE||SS cells, employing the subsequent equation.

$$\sigma = \frac{L}{RS} \quad (2)$$

where the L , R and S stand for the thickness, the bulk resistance and the effective contact area of the *in situ*-based SPEs, respectively. To determine the activation energy of the *in situ*-based SPEs, the logarithm of conductivity and temperature were plotted according to the classical Arrhenius equation:

$$\sigma(T) = A \exp \frac{-E_a}{RT} \quad (3)$$

where $\sigma(T)$ represents the ionic conductivity of In-situ-based SPEs between 20-60 °C, and the pre-exponential factor, the thermodynamic constant, and the test temperature (K) are defined by A , R , and T , respectively. The oxidative stability of *in situ*-based SPEs was studied by testing the cyclic voltammetry curve of Li|SPE|SS cells between 1–6 V. The Li^+ transference number (t_{Li^+}) of synthesized SPEs was tested in Li symmetric cells with *in situ*-based SPEs by the electric potential step method under a polarization time of 6000 s. It was calculated using the following equation:

$$t_{\text{Li}^+} = \frac{I_s(\Delta V - I_0 R_0)}{I_0(\Delta V - I_s R_s)} \quad (4)$$

where I_0 and I_s represent the currents before and after polarization, ΔV is 10 mV, and R_0 and R_s represent the interface resistances of assembled Li symmetrical cells

before and after polarization.

2.6 Cell assembly and testing

The cathode slurry for LiFePO_4 (LFP) and $\text{Ni}_{0.8}\text{Co}_{0.1}\text{Mn}_{0.1}\text{O}_2$ (NCM) was synthesized by combining LFP or NCM, PVDF binder, acetylene black, in a NMP solution with a weight ratio of 8:1:1. Afterwards, the above slurry was applied to Al foil with a doctor blade, and dried at 80°C for 24 h using a vacuum oven. As a final step, the obtained Al foil was cut into 12 mm diameter wafers for further utilization. In addition, the average loading mass of obtained LFP and NCM cathodes in this investigation was approximately 2.0 and 1.8 mg cm^{-2} , respectively. All the cells were assembled using CR2025 coin cells in an argon-filled glove box, with O_2 and water concentrations below 0.1 ppm. For LFP||Li full cells, 1 C corresponds to 170 mA g^{-1} based on the theoretical capacity of LFP. For NCM||Li full cells, 1 C corresponds to 200 mA g^{-1} . The LFP|*In situ*-SL2|Li pouch cell was assembled by LFP cathode, *in situ*-SL2 SPE and thin Li foil in copper foil. The areas of the LFP cathode, *in situ*-SL SPE and thin Li foil were 3.0×3.3 , 3.4×3.5 and $3.2 \times 3\text{ cm}^2$, respectively.

Electrochemical floating experiments were also performed using the LFP|*In situ*-SL2|Li and LFP|*In situ*-SL3|Li cells, which were first charged to 4 V at RT at 0.1 C and then charged at constant voltage for 10 h at each voltage step until 5V.

Galvanostatic charging and discharging tests of all assembled cells were conducted using Neware Batteries Testing System of CT-4008T-5V10mA-164 (Shenzhen, China). The critical current density, short circuit time test, and long cycling tests under different current densities of assembled Li symmetrical cells with *in situ*-based SPEs were tested. The critical current density was examined by incrementally increasing the current density, and each cycle lasted for 40 minutes. During the short circuit time test, the battery was charged at 0.1 mA until a short circuit occurred. The long cycling performances under different current densities (0.1 - 0.5 mA cm^{-2} , and the charging and discharging time being 1 h were also tested. The Cu|Li cell used a nano silver modified copper foil with the diameter of 12 mm on one side and a Li metal piece with the diameter of 14 mm, and investigated at a current density of 0.2 mA cm^{-2} and a constant capacity of 0.4 mA h cm^{-2} . The cycling and rate performances of LFP|SPE|Li and NCM|SPE|Li cells were evaluated under various rates within the 2.5–4.2 V and 3–4.3 V charging and discharging range, respectively.

2.7 Computational methods

Atomistic molecular dynamics simulations were performed in the GROMACS² simulation package (version 2020.6) with the General Amber force field (GAFF2). All structural models contain 4 chains of TFEMA-TFEAA copolymer of 30 repeat units and 42 TFSI molecules. Three concentrations of SL systems were simulated with 21, 84 and 168 SL molecules respectively. The molecules were first randomly placed in cubic boxes of around 6 nm and then solved with the abovementioned number of solvent molecules. After thousands of steps of energy minimization, the systems were equilibrated under the NPT ensemble for 10 ns and followed the production runs of another 10 ns under the canonic ensemble. The temperature was coupled to 298 K using the Nose-Hoover method and the pressure was coupled to 1 atm using the Parrinello-Rahman method. The cutoff scheme of 1.2 nm was implemented for the non-bonded interactions, and the Particle Mesh Ewald method³ with a Fourier spacing of 0.1 nm was applied for the long range electrostatic interactions. All covalent bonds with hydrogen atoms were constraint using the LINCS algorithm⁴.

The Li^+ diffusion coefficient D_{Li^+} is extracted from the slope of the mean squared displacement (MSD) via the Einstein relation for three-dimensional diffusion⁵:

$$D = \frac{1}{6} \frac{d\langle r^2(t) \rangle}{dt} \quad (5)$$

Where $r^2(t)$ is the ensemble-averaged MSD of the ion as a function of time t , the slope of the linear region of the MSD vs. time plot gives $6D$ in three dimensions.

The *ab initio* molecular dynamic (AIMD) simulations were carried out using the Vienna ab initio simulation package (VASP) to understand the reaction mechanism of solvation structure on the Li (001) slab. The Li (001) modeled using a five layered (4×4) slab model. The relaxed Li (001) slab was used to study the interaction. A 15 Å vacuum space was built to model the surface. The kinetic energy cutoff was set at 480 eV⁶. The Brillouin zone was sampled using 1×1×1 Gamma-centered k-point. The AIMD was carried out with spin polarization off for about 100 ps, using a time step of 1 fs.

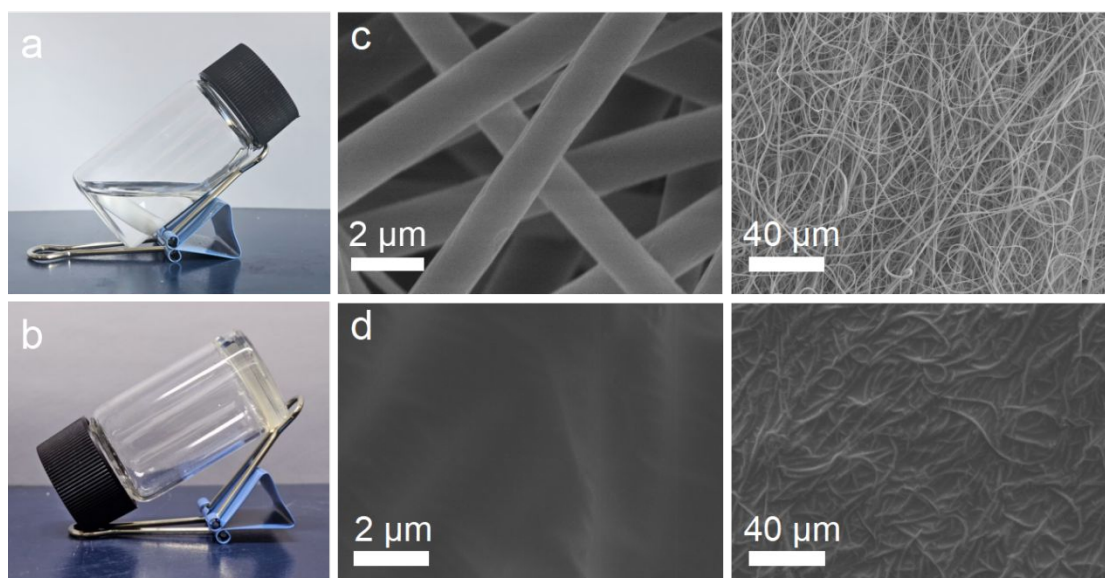


Figure S1. Optical images of the *in situ* solidification process of a) liquid precursor to b) solid polymer electrolyte. SEM images of c) PVDF-HFP/HAP membrane and d) *in situ*-SL2 SPE after polymerization.

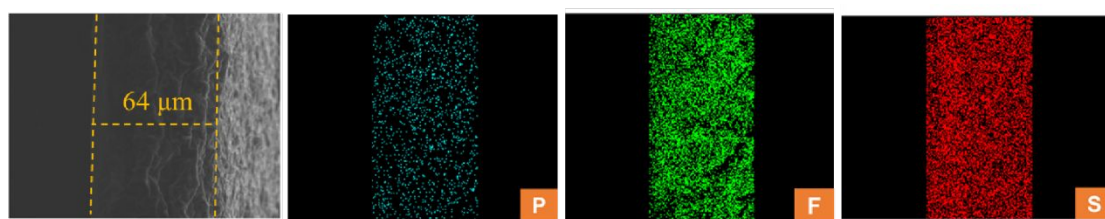


Figure S2. Cross-sectional SEM images of *in situ*-SL2 SPE and corresponding elemental mapping.

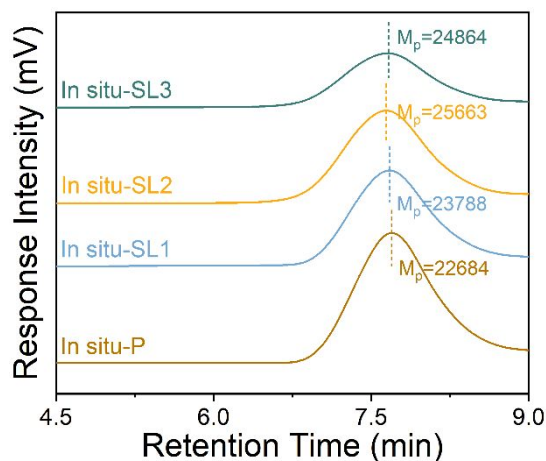


Figure S3. GPC profile of *in situ*-based SPEs.

The degree of polymerization (DP) of In-situ-based SPEs were calculated via the following equation:

$$DP = \frac{M_n}{M_0}$$

where M_p is Peak molecular weight, M_0 is molecular weight of the repeated polymerization unit and M_n is average molecular weight of polymer.

Table S1. Data of GPC analysis for *in situ*-based SPEs.

SPEs	Retention Time (min)	M_0 (g mol ⁻¹)	M_n (g mol ⁻¹)	DP
<i>in situ</i> -P	14.3	322.19	55017	170.75
<i>in situ</i> -SL1	14.4	322.19	53996	167.59
<i>in situ</i> -SL2	14.3	322.19	53247	165.26
<i>in situ</i> -SL3	14.4	322.19	53122	164.87

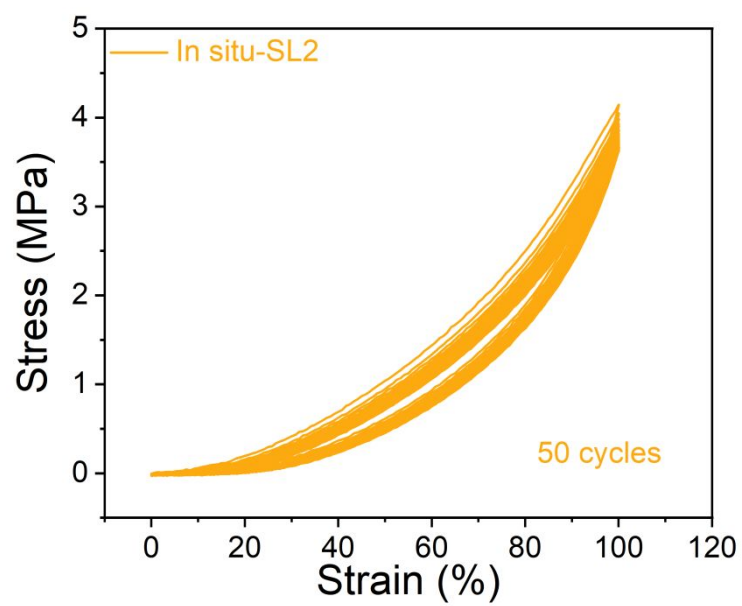


Figure S4. Cyclic tensile testing curves of the *in situ*-SL2 membrane over 50 loading-unloading cycles at 5 mm/min and 100% strain.

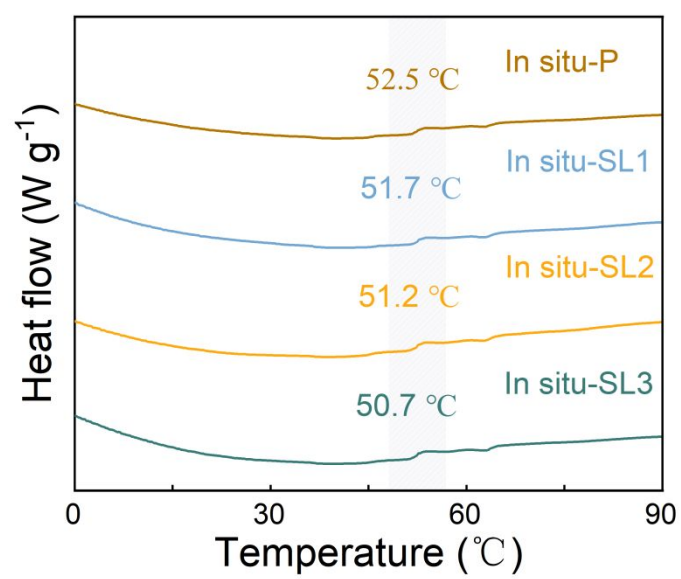


Figure S5. DSC curves of *in situ*-based SPEs.

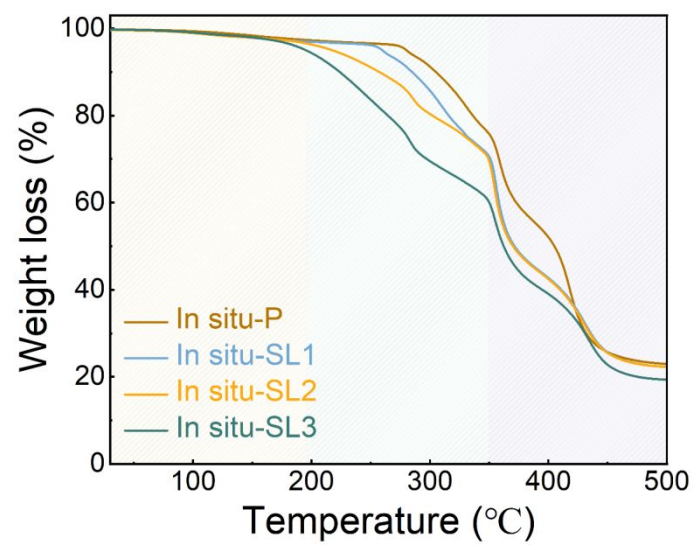


Figure S6. TGA curves of *in situ*-based SPEs.

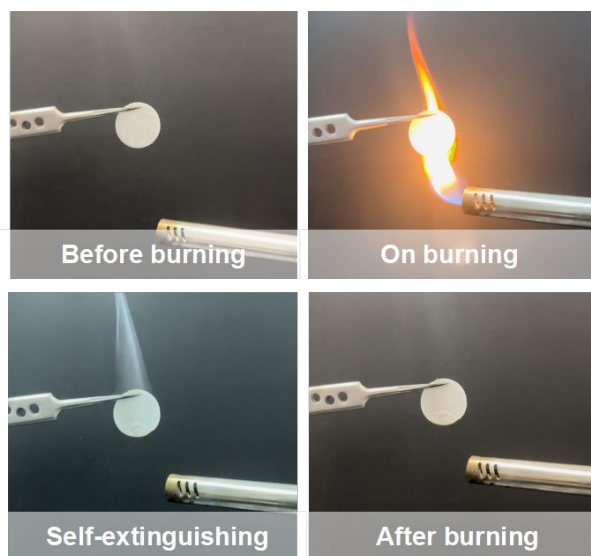


Figure S7. Flammability tests of *in situ*-SL2 SPE.

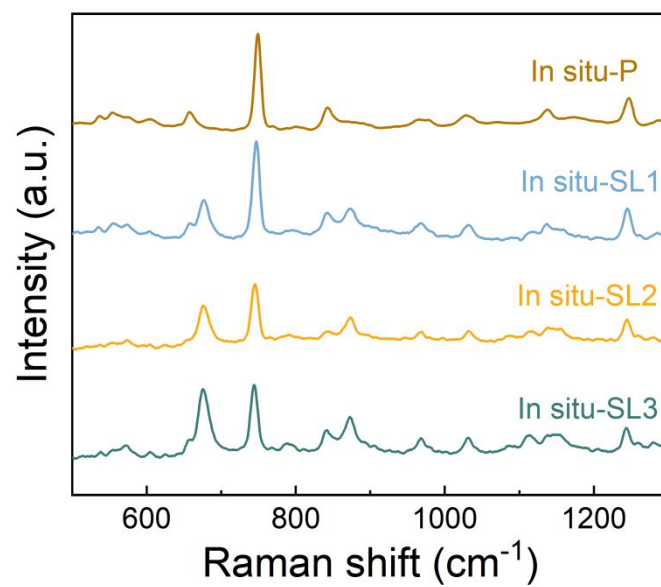


Figure S8. Raman spectra of *in situ*-based SPEs.

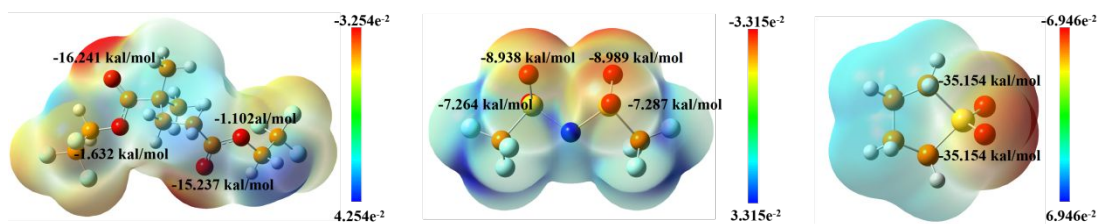


Figure S9. Surface electrostatic potential distribution maps of TFEMA-TFEAA, TFSI⁻ and SL molecules.

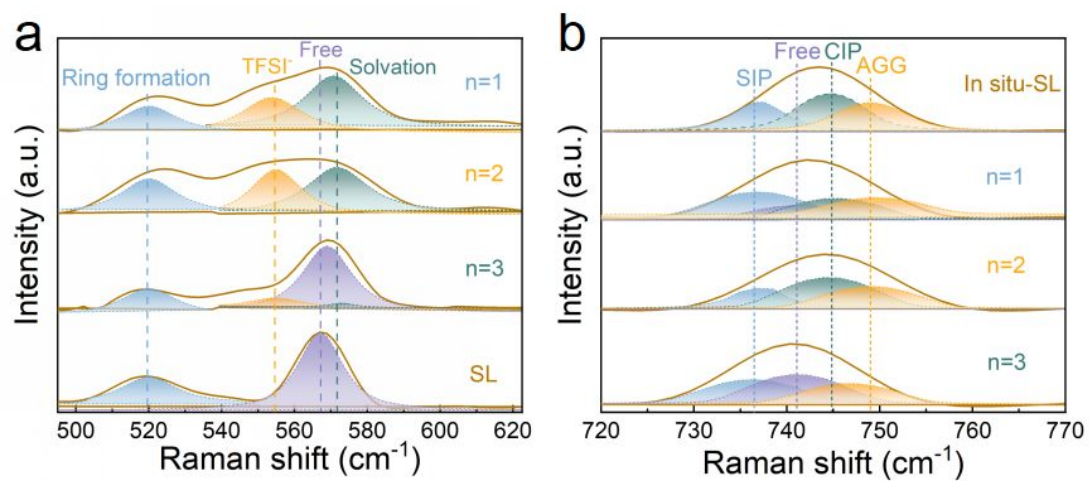


Figure S10. Lorentzian-Gaussian deconvoluted Raman spectra in the range of 500-620 cm^{-1} and 720-770 cm^{-1} .

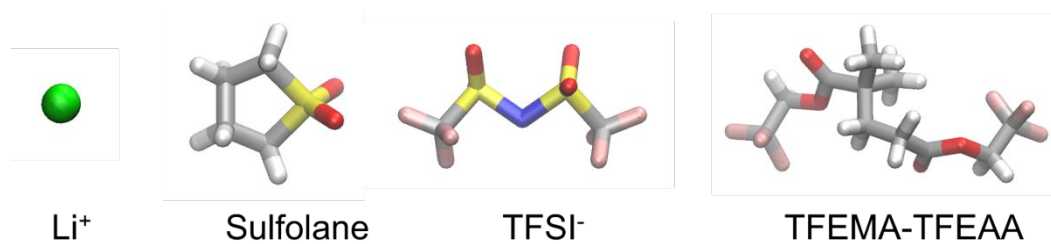


Figure S11. Molecular structures of Li^+ , sulfolane, TFSI^- , and the polymer chain extracted from MD simulations. Color legend: oxygen (yellow), hydrogen (red), carbon (gray), fluorine (white), and lithium (green).

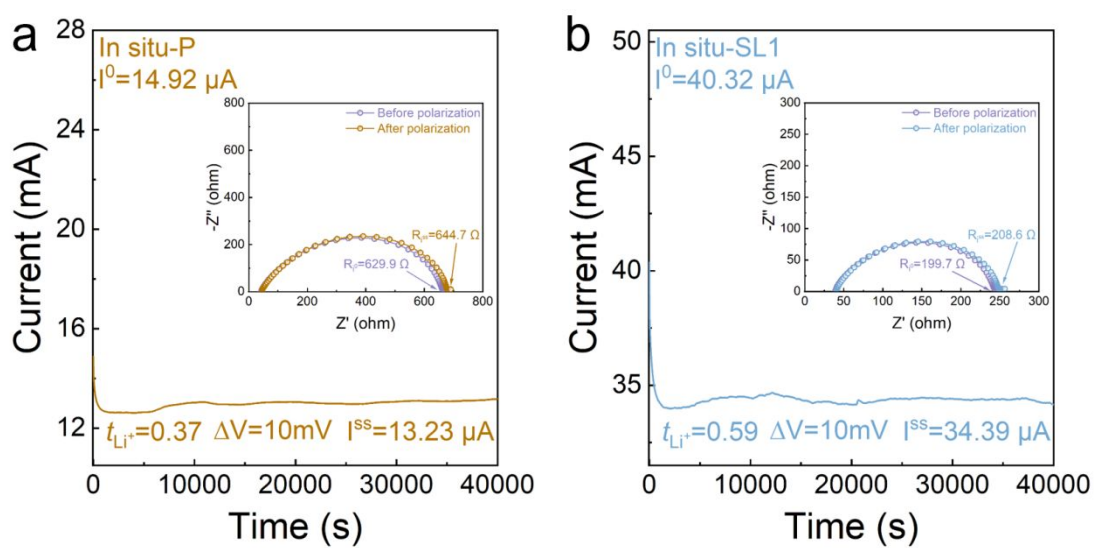


Figure S12. Steady-state chronoamperometry polarization curves under 10 mV polarization voltage with different *in situ*-based SPEs.

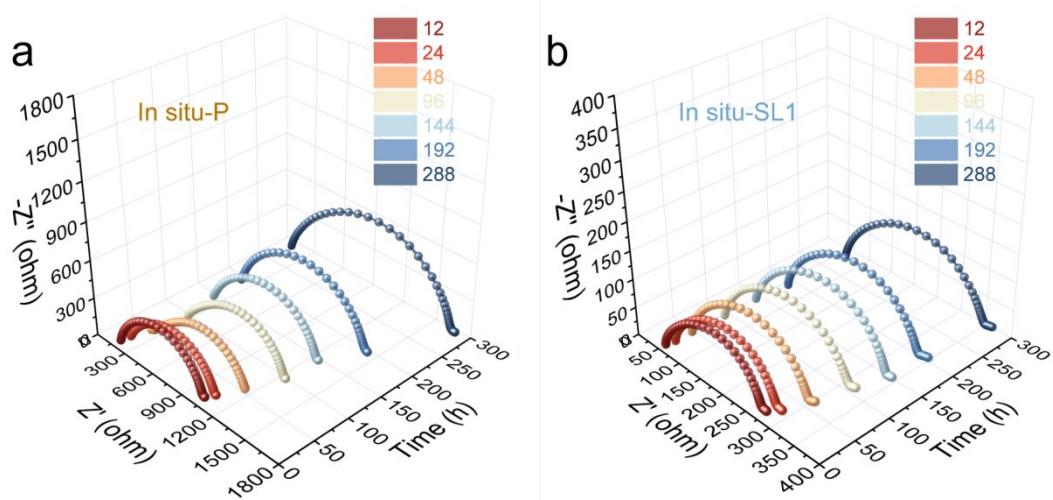


Figure S13. EIS Nyquist plots of Li-symmetric batteries with different *in situ*-based SPEs.

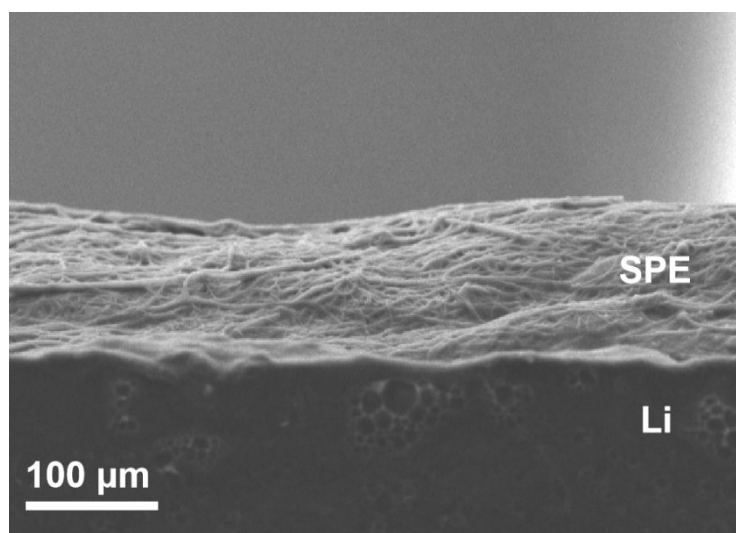


Figure S14. Cross-section SEM images of the interface in Li|*In situ*-SL2|Li cell.

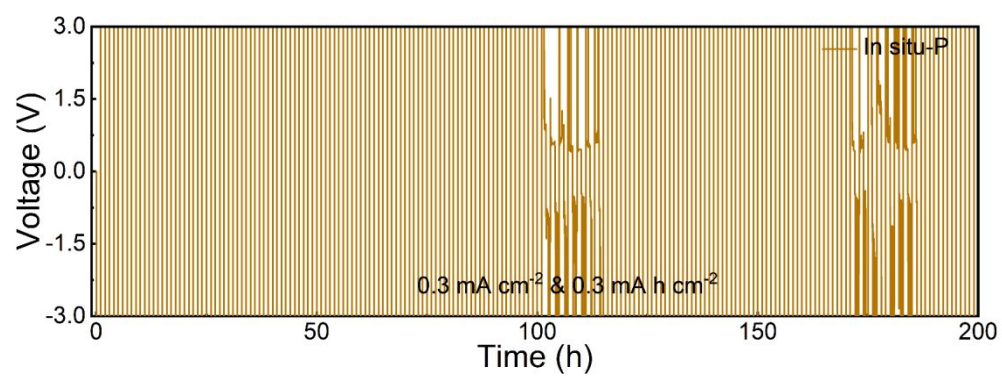


Figure S15. Galvanostatic cycling curves of Li|*In situ*-P|Li cell at 0.3 mA cm⁻² and 0.3 mAh cm⁻².

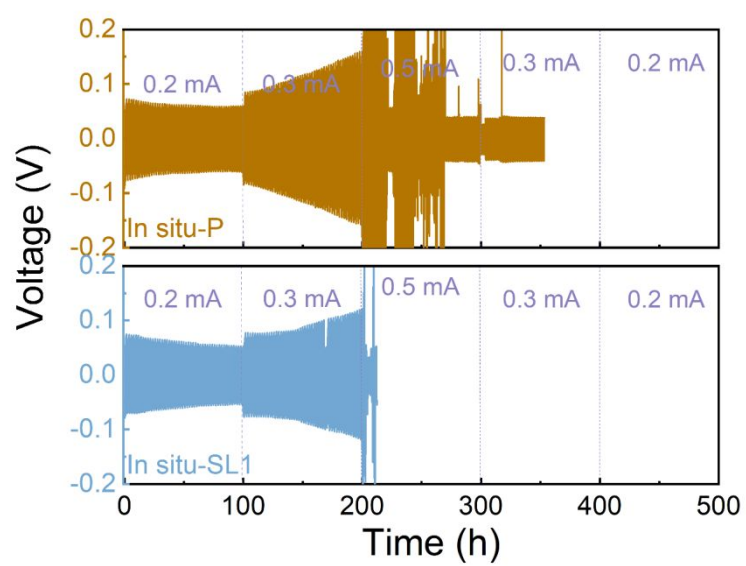


Figure S16. Galvanostatic cycling profile of Li-symmetric cells with *in situ*-based SPEs at 0.2-0.5 mA cm⁻².

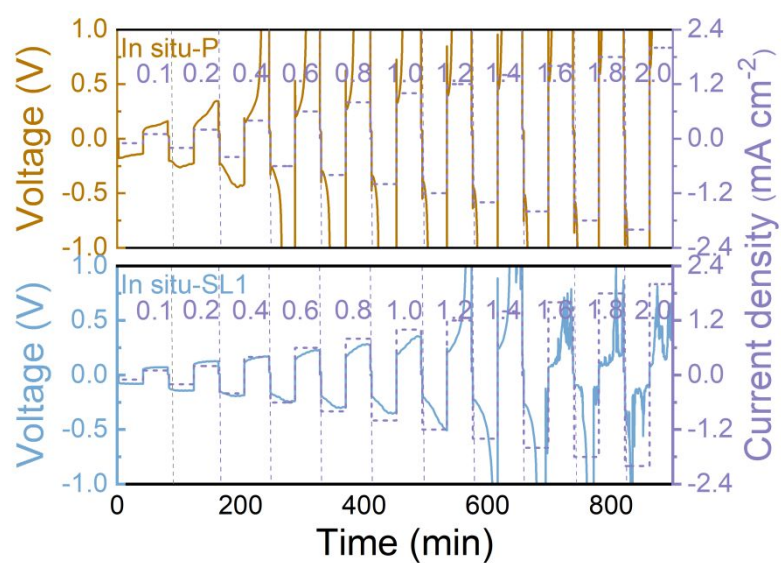


Figure S17. Critical current density (CCD) test under step-up current densities (0.1-2.0 mA cm⁻²) with a constant plating/stripping time of 1 h of *in situ*-based Li-symmetric batteries.

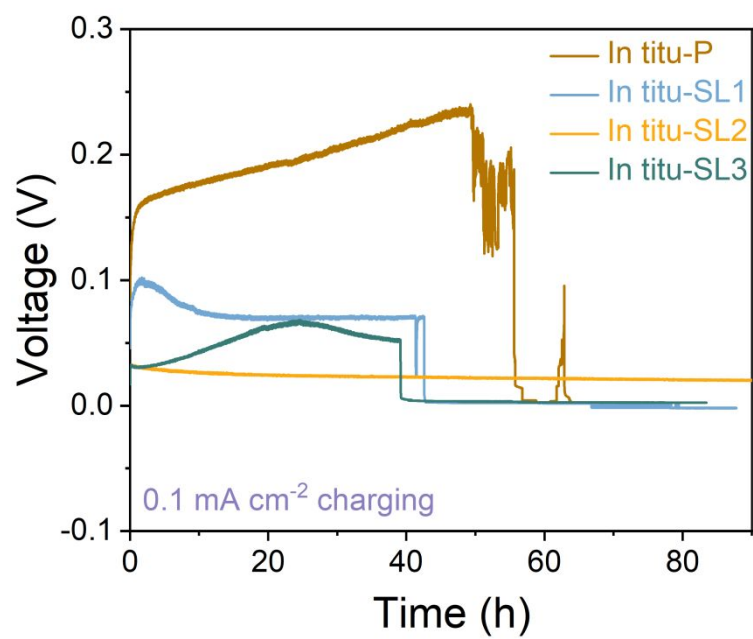


Figure S18. Constant current polarization curves of Li-symmetric cell with current density of 0.1 mA cm⁻² until short circuit occurs.

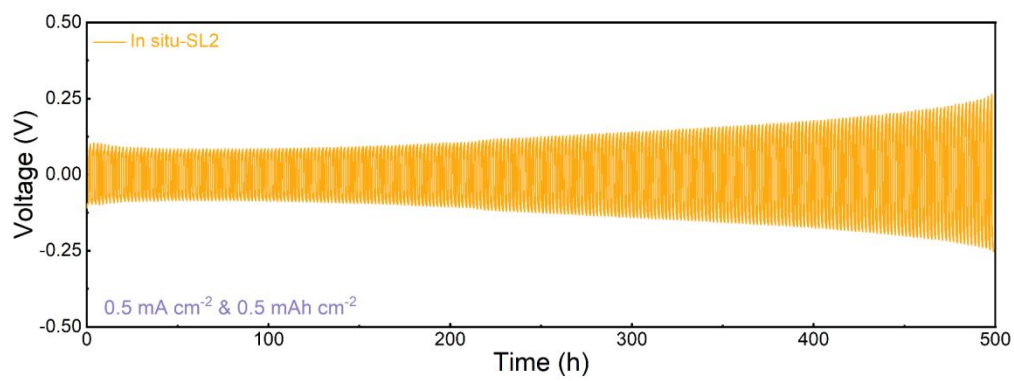


Figure S19. Long-term galvanostatic cycling profile of Li|*In situ*-SL2|Li cell at 0.5 mA cm⁻² and 0.5 mAh cm⁻².

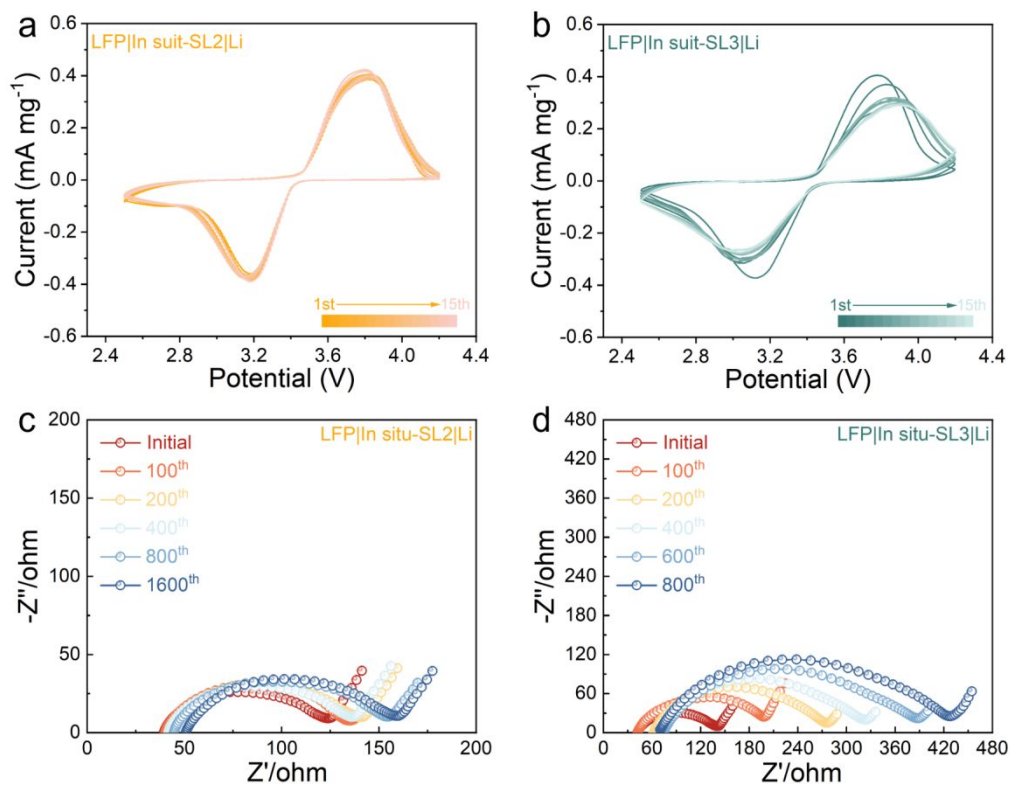


Figure S20. Cyclic voltammetric (CV) curves of a) LFP/*In situ*-SL2|Li cells and b) LFP/*In situ*-SL3|Li cells. EIS Nyquist plots of c) LFP/*In situ*-SL2|Li cells during cycling and d) LFP/*In situ*-SL3|Li cell during cycling.

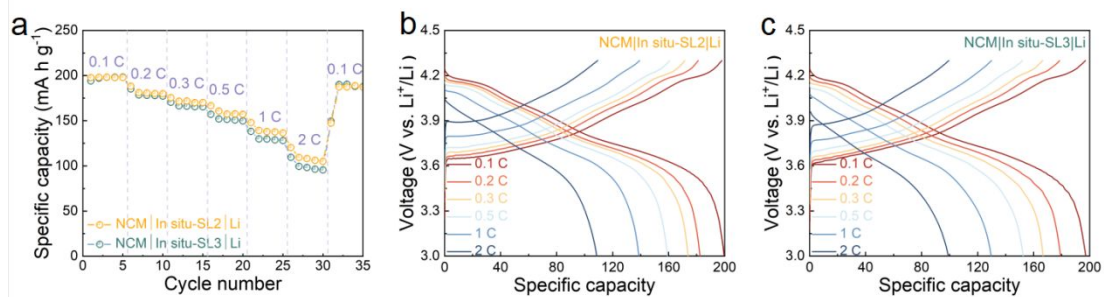


Figure S21. Rate performance of the NCM|*In situ*-SL2|Li and NCM|*In situ*-SL3|Li cells at different C-rates. Charge/discharge profiles at different rates of b) *in situ*-SL2 and c) *in situ*-SL3 based NCM||Li cells.

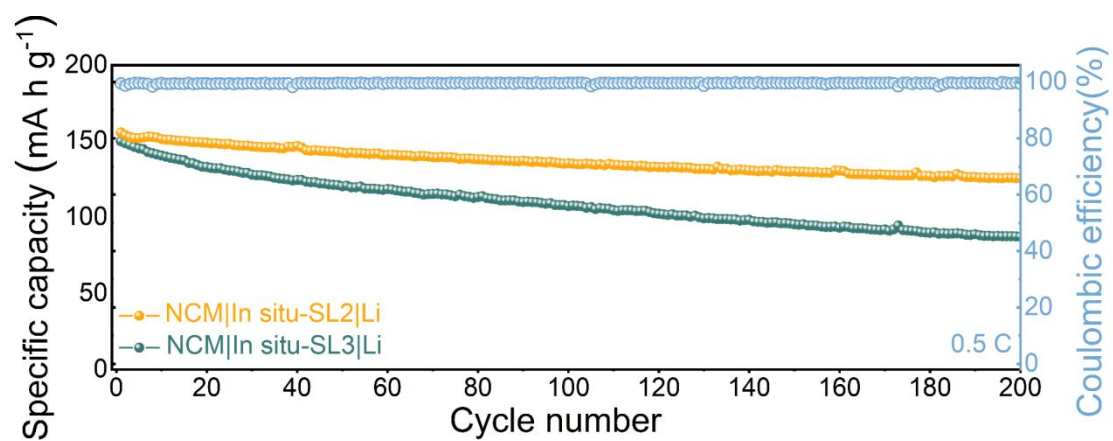


Figure S22. Cycling performance of NCM||Li cells using different electrolytes at 0.5 C.

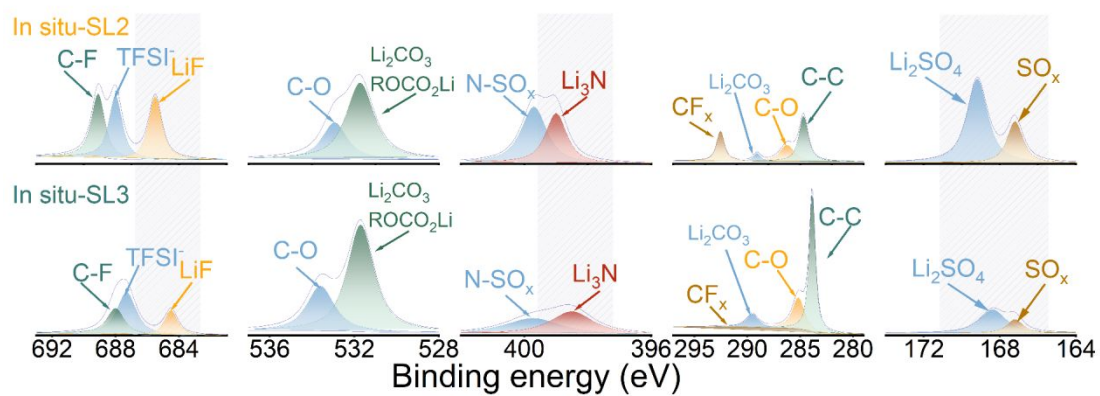


Figure S23. Elemental analysis of the NCM surface after 10 cycles from cycled NCM||Li cells incorporating *in situ*-SL2 and *in situ*-SL3 SPEs.

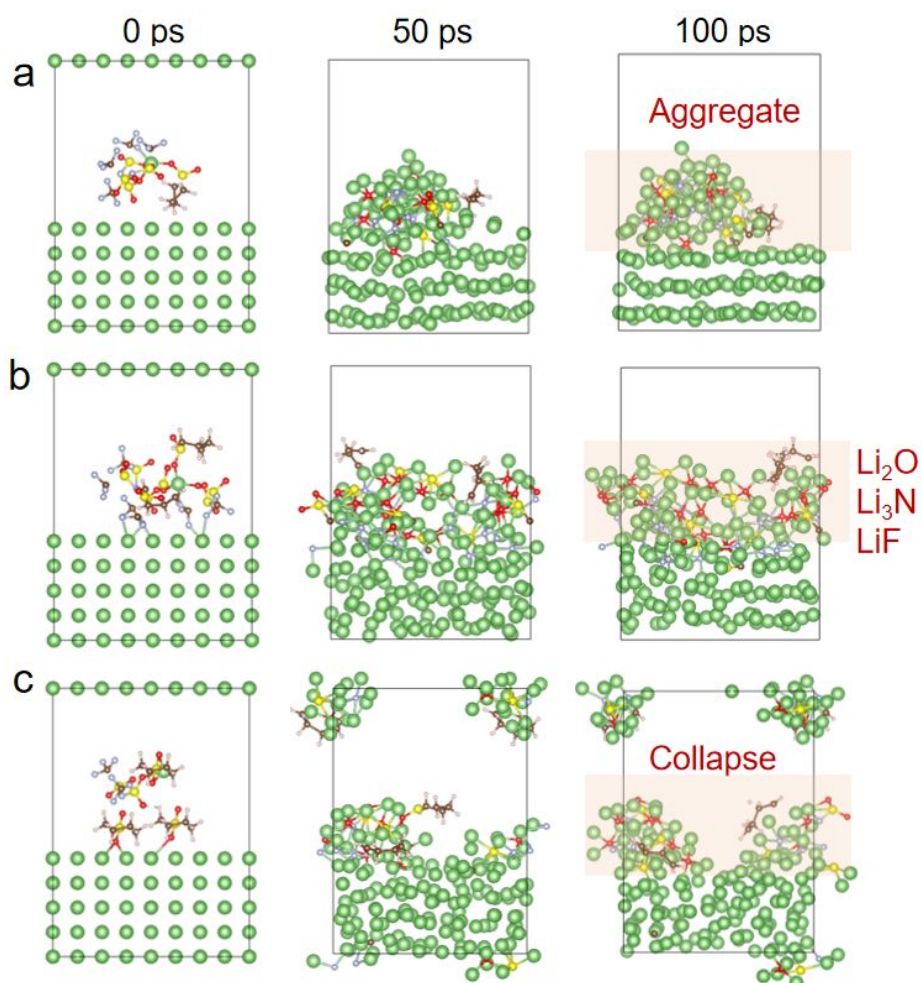


Figure S24. *Ab initio* molecular dynamic (AIMD) simulations of interface reaction and SEI formation on Li metal of a) *in situ*-SL1, b) *in situ*-SL2 and c) *in situ*-SL3 systems.

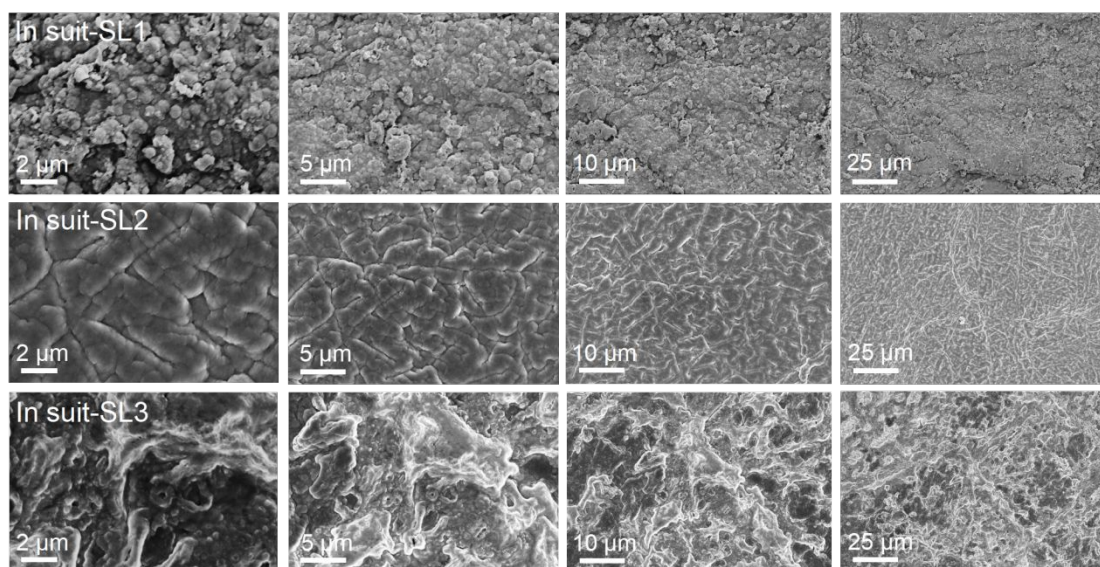


Figure S25. SEM images of the Li anode surface obtained from cycled LFP||Li symmetric cells assembled with the *in situ*-based SPEs.

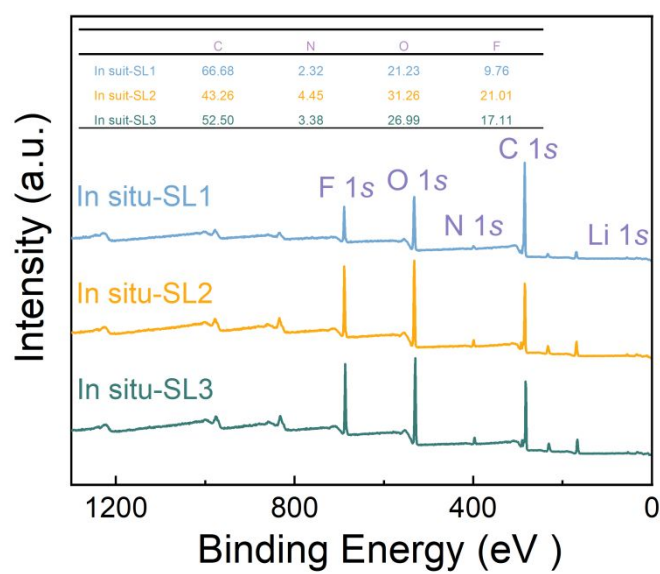


Figure S26. XPS wide spectra of the Li anode surface obtained from cycled LFP||Li symmetric cells assembled with the *in situ*-based SPEs (inset: the corresponding elemental contents).

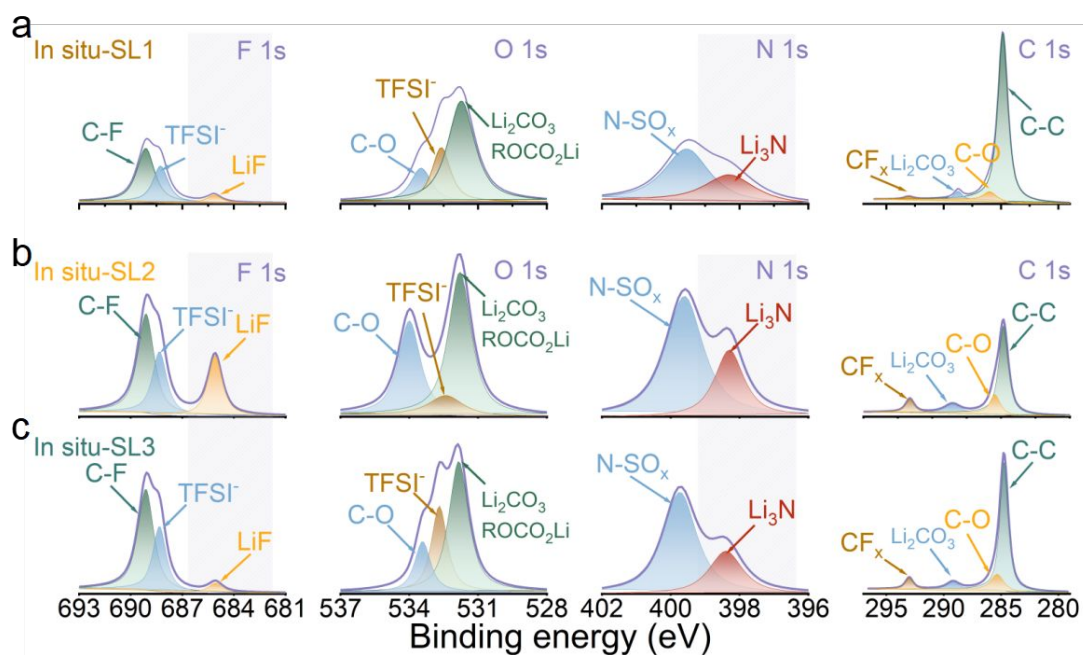


Figure S27. Elemental analysis of the Li anode surface obtained from cycled LFP||Li symmetric cells assembled with the *in situ*-based SPEs.

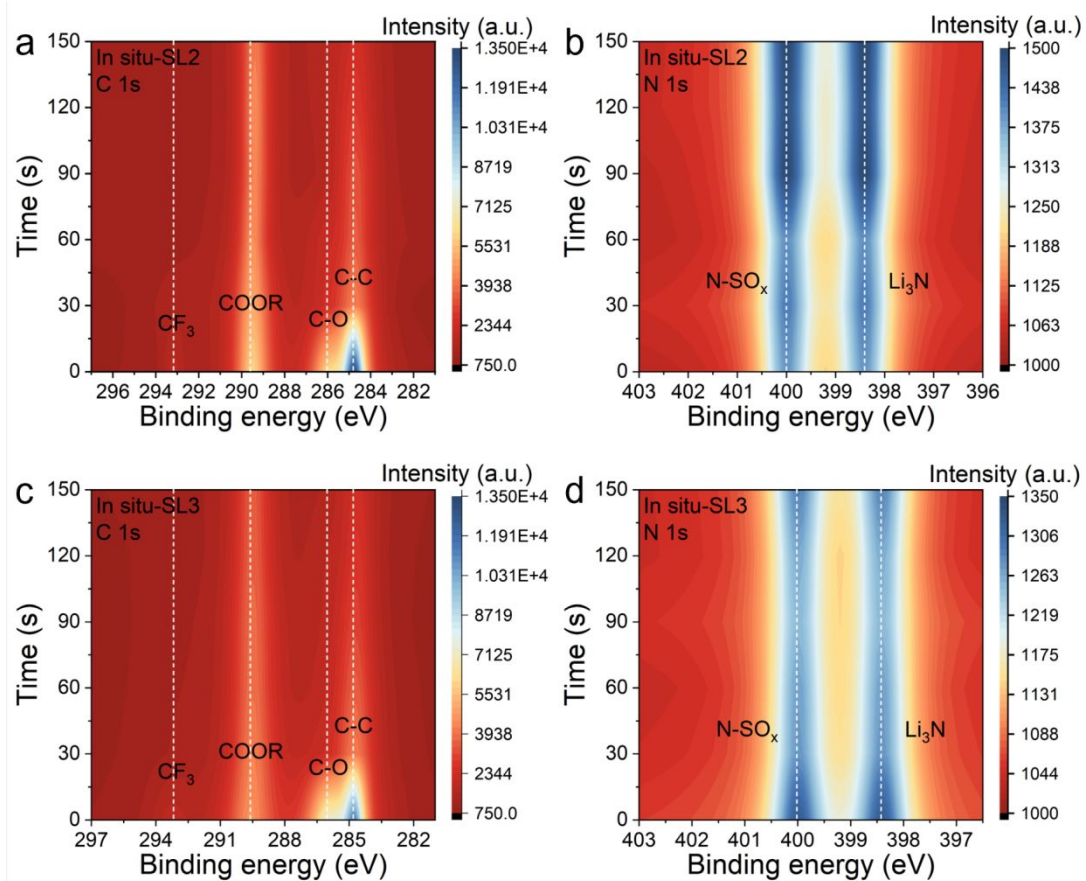


Figure S28. XPS depth profiles of C 1s and N 1s in the SEI of cycled LFP/*In situ*-SL2/Li and LFP/*In situ*-SL3/Li cells at 1 C after 20 cycles.

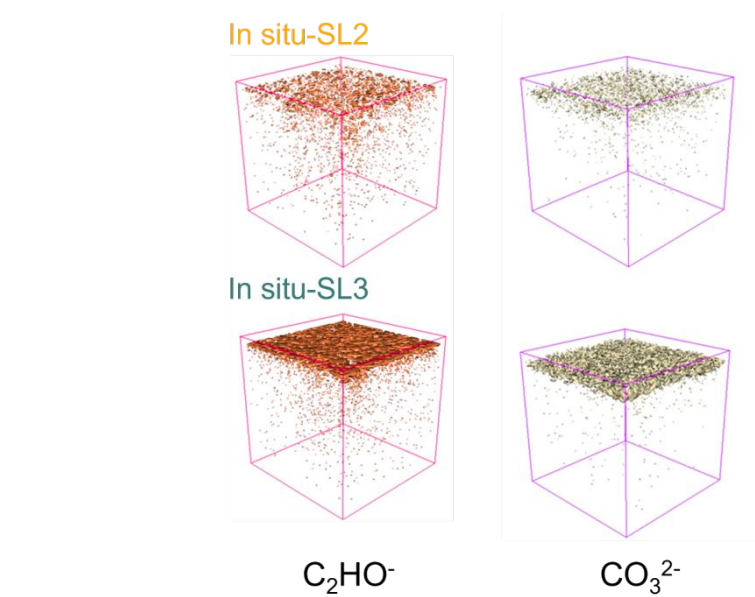


Figure S29. 3D TOF-SIMS mappings for the cycled LFP/*In situ*-SL2|Li and LFP/*In situ*-SL3|Li cells after 10 cycles.

Table S2. Comparison of the cycling stability of LFP cells with different polymer electrolytes in previous work.

Electrolytes	Rate	Cycles	Capacity retention	Loading mass (mg/cm ²)	Cut-off voltage (V)	Temperature (°C)	Ref.
PEGDA/DME	0.5C	600	77.4%	2	4.2	25	1 ⁷
PDOL-TGIC	1 C	400	92.5%	3	4.2	25	2 ⁸
TM/TMS-TFEC	2 C	2000	82.6%	2	4.2	25	3 ⁹
BA/NMP	0.2 C	370	80.0%	2	4.2	25	4 ¹⁰
FCDOL	1 C	1000	82.8%	3	4.2	25	5 ¹¹
TA	0.5 C	400	82.5%	7	4.2	25	6 ¹²
PEGDME-PMMA	0.5 C	2000	86.0%	2	4.2	25	7 ¹³
PVC/LSC	2 C	500	78.0%	2	4.2	25	8 ¹⁴
Acrylate-VEC	1 C	900	81.8%	1.5	4.2	40	9 ¹⁵
P-LLCTO/PAN	0.5 C	1000	82.3 %	2	4.2	25	10 ¹⁶
TA-PEO	70 mA g ⁻¹	200	91.0%	LMFP	4.2	25	11 ¹⁷
PDOL-CNTs	0.2 C	150	69.0%	2	4.2	25	12 ¹⁸
PDOL/YSZ-Al(CF ₃ SO ₃) ₃	2 C	600	92.1%	1.2	4.2	25	13 ¹⁹
PDOL/LiNO ₃ -TEGDN	1 C	2000	89.4%	1.8	4.2	23	14 ²⁰
<i>in situ</i> -SL2	3 C	2000	91.7%	2	4.2	25	This work

References

- (1) Sinnaeve, D. The Stejskal–Tanner Equation Generalized for Any Gradient Shape—an Overview of Most Pulse Sequences Measuring Free Diffusion. *Concept. Magn. Reson.* **2012**, *40A* (2), 39–65. <https://doi.org/10.1002/cmr.a.21223>.
- (2) Hess, B.; Kutzner, C.; van der Spoel, D.; Lindahl, E. GROMACS 4: Algorithms for Highly Efficient, Load-Balanced, and Scalable Molecular Simulation. *J. Chem. Theory Comput.* **2008**, *4* (3), 435–447. <https://doi.org/10.1021/ct700301q>.
- (3) Essmann, U.; Perera, L.; Berkowitz, M. L.; Darden, T.; Lee, H.; Pedersen, L. G. A Smooth Particle Mesh Ewald Method. *Chem. Phys.* **1995**, *103* (19), 8577–8593. <https://doi.org/10.1063/1.470117>.
- (4) Hess, B.; Bekker, H.; Berendsen, H. J. C.; Fraaije, J. G. E. M. LINCS: A Linear Constraint Solver for Molecular Simulations. *J. Comput. Chem.* **1997**, *18* (12), 1463–1472. [https://doi.org/10.1002/\(SICI\)1096-987X\(199709\)18:12<1463::AID-JCC4>3.0.CO;2-H](https://doi.org/10.1002/(SICI)1096-987X(199709)18:12<1463::AID-JCC4>3.0.CO;2-H).
- (5) Liu, X.; Schnell, S. K.; Simon, J.-M.; Krüger, P.; Bedeaux, D.; Kjelstrup, S.; Bardow, A.; Vlugt, T. J. H. Diffusion Coefficients from Molecular Dynamics Simulations in Binary and Ternary Mixtures. *Int. J. Thermophys* **2013**, *34* (7), 1169–1196. <https://doi.org/10.1007/s10765-013-1482-3>.
- (6) Ong, S. P.; Mo, Y.; Richards, W. D.; Miara, L.; Lee, H. S.; Ceder, G. Phase Stability, Electrochemical Stability and Ionic Conductivity of the $\text{Li}_{10\pm1}\text{MP}_2\text{X}_{12}$ (M = Ge, Si, Sn, Al or P, and X = O, S or Se) Family of Superionic Conductors. *Energy Environ. Sci.* **2013**, *6* (1), 148–156. <https://doi.org/10.1039/C2EE23355J>.
- (7) Zhou, M.; Chen, W.; Yang, H.; Hu, Y.; Lei, T.; Chen, D.; Wang, S.; Zhang, Y.; Xiong, J. Molecular Crowding Solid Polymer Electrolytes for Lithium Metal Battery by In Situ Polymerization. *Adv. Energy Mater.* **2025**, *15* (5), 2403082. <https://doi.org/10.1002/aenm.202403082>.
- (8) Yang, S.; Yuan, H.; Yao, N.; Hu, J.; Wang, X.; Wen, R.; Liu, J.; Huang, J. Intrinsically Safe Lithium Metal Batteries Enabled by Thermo-Electrochemical Compatible In Situ Polymerized Solid-State Electrolytes. *Adv. Mater.* **2024**, *36* (35), 2405086. <https://doi.org/10.1002/adma.202405086>.
- (9) Lv, Q.; Li, C.; Liu, Y.; Jing, Y.; Sun, J.; Wang, H.; Wang, L.; Ren, H.; Wu, B.; Cheng, T.; Wang, D.; Liu, H.; Dou, S.-X.; Wang, B.; Wang, J. In-Situ Polymerized High-Voltage Solid-State Lithium Metal Batteries with Dual-Reinforced Stable Interfaces. *ACS Nano* **2024**, *18* (34), 23253–23264. <https://doi.org/10.1021/acsnano.4c06057>.
- (10) Wang, S.; Lv, Q.; Jing, Y.; Wang, B.; Wang, D.; Liu, H.; Dou, S. In Situ Polymerization Design of a Quasi-Solid Electrolyte Enhanced by NMP Additive for Lithium Metal Batteries. *Energy Storage Mater.* **2024**, *69*, 103390. <https://doi.org/10.1016/j.ensm.2024.103390>.
- (11) Li, J.; Li, C.; Yao, Y.; Li, Z.; Yao, J.; Luo, L.; Liao, W.; Ye, X.; Dai, W.; Li, F.; Zhang, X.; Xiang, Y. In Situ Polymerized Flame-Retardant Crosslinked Quasi Solid-State Electrolytes for High-Voltage Lithium Metal Batteries. *Adv. Energy*

- Mater.* **2024**, *14* (42), 2402362. <https://doi.org/10.1002/aenm.202402362>.
- (12) Xu, H.; Deng, W.; Shi, L.; Long, J.; Zhang, Y.; Xu, L.; Mai, L. The Role of the Molecular Encapsulation Effect in Stabilizing Hydrogen-Bond-Rich Gel-State Lithium Metal Batteries. *Angew. Chem. Int. Ed.* **2024**, *63* (27), e202400032. <https://doi.org/10.1002/anie.202400032>.
 - (13) Tong, R.-A.; Huang, Y.; Feng, C.; Dong, Y.; Wang, C.-A. In-Situ Polymerization Confined PEGDME-Based Composite Quasi-Solid-State Electrolytes for Lithium Metal Batteries. *Adv. Funct. Mater.* **2024**, *34* (30), 2315777. <https://doi.org/10.1002/adfm.202315777>.
 - (14) Jin, Y.; Lin, R.; Li, Y.; Zhang, X.; Tan, S.; Shuai, Y.; Xiong, Y. Revealing the Influence of Electron Migration Inside Polymer Electrolyte on Li⁺ Transport and Interphase Reconfiguration for Li Metal Batteries. *Angew. Chem. Int. Ed.* **2024**, *63* (24), e202403661. <https://doi.org/10.1002/anie.202403661>.
 - (15) Qin, S.; Yu, Y.; Zhang, J.; Ren, Y.; Sun, C.; Zhang, S.; Zhang, L.; Hu, W.; Yang, H.; Yang, D. Separator-Free In Situ Dual-Curing Solid Polymer Electrolytes with Enhanced Interfacial Contact for Achieving Ultrastable Lithium-Metal Batteries. *Adv. Energy Mater.* **2023**, *13* (34), 2301470. <https://doi.org/10.1002/aenm.202301470>.
 - (16) Jin, Y.; Li, Y.; Lin, R.; Zhang, X.; Shuai, Y.; Xiong, Y. In Situ Constructing Robust and Highly Conductive Solid Electrolyte with Tailored Interfacial Chemistry for Durable Li Metal Batteries. *Small* **2024**, *20* (19), 2307942. <https://doi.org/10.1002/sml.202307942>.
 - (17) Su, Y.; Rong, X.; Gao, A.; Liu, Y.; Li, J.; Mao, M.; Qi, X.; Chai, G.; Zhang, Q.; Suo, L.; Gu, L.; Li, H.; Huang, X.; Chen, L.; Liu, B.; Hu, Y.-S. Rational Design of a Topological Polymeric Solid Electrolyte for High-Performance All-Solid-State Alkali Metal Batteries. *Nat. Commun.* **2022**, *13* (1), 4181. <https://doi.org/10.1038/s41467-022-31792-5>.
 - (18) Mi, Y. Q.; Deng, W.; He, C.; Eksik, O.; Zheng, Y. P.; Yao, D. K.; Liu, X. B.; Yin, Y. H.; Li, Y. S.; Xia, B. Y.; Wu, Z. P. In Situ Polymerized 1,3-Dioxolane Electrolyte for Integrated Solid-State Lithium Batteries. *Angew. Chem. Int. Ed.* **2023**, *62* (12), e202218621. <https://doi.org/10.1002/anie.202218621>.
 - (19) Mu, K.; Wang, D.; Dong, W.; Liu, Q.; Song, Z.; Xu, W.; Yao, P.; Chen, Y.; Yang, B.; Li, C.; Tian, L.; Zhu, C.; Xu, J. Hybrid Crosslinked Solid Polymer Electrolyte via In-Situ Solidification Enables High-Performance Solid-State Lithium Metal Batteries. *Adv. Mater.* **2023**, *35* (47), 2304686. <https://doi.org/10.1002/adma.202304686>.
 - (20) Wang, Z.; Wang, Y.; Shen, L.; Jin, Z.; Law, H. M.; Wang, A.; Wang, W.; Ciucci, F. Towards Durable Practical Lithium–Metal Batteries: Advancing the Feasibility of Poly-DOL-Based Quasi-Solid-State Electrolytes via a Novel Nitrate-Based Additive. *Energy Environ. Sci.* **2023**, *16* (9), 4084–4092. <https://doi.org/10.1039/D3EE02020G>.